Graphene Technology
https://doi.org/10.1007/s41127-019-00024-x

ORIGINAL ARTICLE

Improved DSSC photovoltaic performance using reduced graphene oxide–carbon nanotube/platinum assisted with customised triple-tail surfactant as counter electrode and zinc oxide nanowire/titanium dioxide nanoparticle bilayer nanocomposite as photoanode

Suriani Abu Bakar[1,2] · Fatiatun[1,2] · Azmi Mohamed[1,3] · Muqoyyanah[1,2] · Norhayati Hashim[1,3] · Mohamad Hafiz Mamat[4,5] · Mohd Khairul Ahmad[6] · Putut Marwoto[7]

Received: 10 September 2018 / Revised: 7 January 2019 / Accepted: 6 March 2019

Abstract
In this work, reduced graphene oxide (rGO) was produced from graphene oxide (GO) by a reduction process, which utilised hydrazine hydrate as reducing agent. GO was initially synthesised by electrochemical exfoliation assisted with customised triple-tail sodium 1,4-bis(neopentyloxy)-3-(neopentyloxycarbonyl)-1,4-dioxobutane-2-silphonate (TC14) surfactant. The produced TC184-rGO solution was subsequently hybridised with multiwalled carbon nanotubes (MWCNTs) from waste palm oil. The produced TC14-rGO and TC14-rGO/MWCNTs hybrid solution was fabricated as thin films by spray coating method. Afterwards, Pt nanoparticle (NP) coating was fabricated. The films were used as counter electrode (CE) for dye-sensitised solar cell (DSSC) application. Three other CEs, namely TC14-rGO, TC14-rGO/MWCNTs hybrid and TC14-rGO/Pt hybrid, were fabricated for comparison. Zinc oxide nanowire (NWR)/titanium dioxide nanoparticle (NP) bilayer was utilised as photoanode and fabricated via sol–gel immersion and squeegee method. Solar simulator measurement showed that the highest DSSC performance was exhibited by TC14-rGO/MWCNTs/Pt hybrid, which presented an energy conversion efficiency, open-circuit voltage, short-circuit-current density and fill factor of 0.0842%, 0.608 V, 0.285 mA/cm^2 and 0.397, respectively. The combination of TC14-rGO/MWCNTs/Pt hybrid CE and ZnO NWR/TiO_2 NP bilayer photoanode improved the DSSC performance due to the large surface area of TC14-rGO and MWCNTs, the high electrical conductivity of MWCNTs and the high quality and less agglomeration of thin rGO film assisted with triple-tail TC14 surfactant. The ZnO NWR/TiO_2 NP bilayer photoanode also demonstrated a large surface area that can optimally adsorb dye molecules and increase the photo-exciton electrons, which further improve the DSSC performance.

Keywords Electrochemical exfoliation · Reduced graphene oxide · Multiwalled carbon nanotubes/platinum hybrid · Counter electrode · Zinc oxide nanowire/titanium dioxide nanoparticle bilayer · Dye-sensitised solar cells

✉ Suriani Abu Bakar
absuriani@yahoo.com

[1] Faculty of Science and Mathematics, Nanotechnology Research Centre, Universiti Pendidikan Sultan Idris, 35900 Tanjung Malim, Perak, Malaysia

[2] Department of Physics, Faculty of Science and Mathematics, Universiti Pendidikan Sultan Idris, 35900 Tanjung Malim, Perak, Malaysia

[3] Department of Chemistry, Faculty of Science and Mathematics, Universiti Pendidikan Sultan Idris, 35900 Tanjung Malim, Perak, Malaysia

[4] Faculty of Electrical Engineering, NANO-Electronic Centre (NET), Universiti Teknologi MARA (UiTM), 40450 Shah Alam, Selangor, Malaysia

[5] NANO-SciTech Centre (NST), Institute of Science (IOS), Universiti Teknologi MARA (UiTM), 40450 Shah Alam, Selangor, Malaysia

[6] Faculty of Electrical and Electronic Engineering, Microelectronic and Nanotechnology-Shamsuddin Research Centre (MiNT-SRC), Universiti Tun Hussein Onn Malaysia, 86400 Parit Raja, Batu Pahat, Johor, Malaysia

[7] Materials Research Group, Thin Film Laboratory, Faculty of Mathematics and Natural Science, Universitas Negeri Semarang (UNNES), Sekaran Gunungpati, Semarang 50229, Indonesia

Published online: 15 March 2019

1 Introduction

Since 1991, dye-sensitised solar cells (DSSC) have been the most popular third-generation solar cells, and they are widely developed as alternatives to silicon-based solar cells because of their advantages of simple fabrication, high-energy-conversion efficiency (η), environmental safety and low production cost [1–3]. DSSC also perform better than conventional solar cells, and they can convert solar energy to electricity. DSSC consist of four components: photoanode, dye, electrolyte and counter electrode (CE). DSSC application has obtained considerable attention due to its role as a mediator in generating a sensitiser after electron injection and its key role in regulating the DSSC device performance [4].

Graphene is a promising alternative for Pt [5] due to its excellent properties, such as high thermal and electrical conductivity [6, 7], high chemical and mechanical robustness [8] and high surface area (2630 $m^2 g^{-1}$) [9, 10]. Graphene also presents low production cost, simple preparation, high optical transparency, good electrocatalytic activity, environmental safety and high η for DSSC application [4, 11, 12]. Graphene can be synthesised by using physical approaches, such as micromechanical exfoliation, epitaxial growth on silicon carbide and chemical vapour deposition (CVD) [13]. CVD exhibits low efficiency and high energy consumption because the synthesis process requires a high temperature of ~ 1000 °C [13].

Platinum is widely used as a CE because of its high conductivity and catalytic activity [14]. Unfortunately, Pt is expensive, corrosive in liquid electrolyte and limited in nature. Thus, Pt usage must be replaced and reduced. Carbonaceous materials, such as graphene [5], multiwalled carbon nanotubes (MWCNTs) [15] and carbon black [16], are preferred alternative CE materials for conventional Pt CE films. In addition to graphene, its derivative graphene oxide (GO) has been developed as a CE material due to its easy fabrication, high electrical conductivity and large surface area [17]. GO can be synthesised through chemical approaches, such as Hummers' method [18] and electrochemical exfoliation [19]. Hummers' method presents high cost production due to high chemical consumption and long production time [20]. Therefore, the electrochemical exfoliation is preferred for GO synthesis because of its environmental safety, less chemical content, simplicity and low production cost. This method also shows potential for large-scale production in single synthesis time [21].

Several solvents, such as dimethylformamide, propylene carbonate, acetonitrile, nitric acid and sulphuric acid [22, 23], are commonly used as electrolytes during electrochemical exfoliation. However, water-based electrolytes are more environmentally friendly than acidic and sulphuric electrolytes [24]. In water-based electrolytes, a surfactant plays a key role in electrochemical exfoliation for intercalation process and consequently determines the quality of produced GO [25]. Surfactants are also used as stabilisers and dispersing agents for the exfoliated GO [26]. Several kinds of surfactants, such as commercially available single-tail sodium dodecylbenzene sulphonate (SDBS) [27], single-tail sodium dodecyl sulphate (SDS) [28] and single-tail poly(sodium 4-styrenesulfonate) [29], are commonly used to assist in GO synthesis. Single-tail SDBS and SDS surfactants are also used to disperse MWCNTs in natural rubber latex (NRL), which is utilised to reduce the interfacial tension in MWCNTs-NRL nanocomposites [25, 30, 31]. Single-tail SDS and customised triple-tail sodium 1,4-bis(neopentyloxy)-3-(neopentyloxycarbonyl)-1,4-dioxobutane-2-silphonate (TC14) surfactants were previously used to assist in the GO synthesis; the TC14 surfactant achieves better exfoliation process than that of single-tail SDS, thereby presenting less agglomeration and higher electrical conductivity of produced TC14-GO [24].

In the current study, a customised triple-tail TC14 surfactant was also used to assist the GO synthesis due to its better exfoliation process than that of single-tail surfactant. The customised triple-tail TC14 surfactant offers triple interaction, which achieves good exfoliation process and dispersal and produces high-quality GO. The produced TC14-GO was subsequently reduced by utilising hydrazine hydrate as reducing agent to produce reduced GO (rGO). Hydrazine hydrate is preferred because of its better performance to reduce oxygen content and produce fine rGO [32] than those of other reducing agents, such as sugar [33], heparin [34], protein bovine serum albumin [35] and polydiallyldimethylammonium chloride [36].

The produced TC14-rGO was combined with Pt and other carbonaceous materials, such as MWCNTs, due to that its sp^2 structure is similar to them. MWCNTs also show high chemical stability, electrical conductivity, mechanical properties and thermal conductivity [37–39]. According to the roll wall number, CNTs possess three structures, including SWCNTs [40, 41], MWCNTs [41–43] and double-walled carbon nanotubes [44]. SWCNTs and MWCNTs structures are widely developed as CEs for DSSC application because of their good electronic properties. In the current study, MWCNTs from waste palm oil (WPO) [45] were composited with the TC14-rGO and Pt to form TC14-rGO/MWCNTs and TC14-rGO/MWCNTs/Pt hybrids as CE thin films due to their lower production cost than those of other MWCNTs from conventional precursors and SWCNTs. The TC14-rGO and MWCNTs from WPO were utilised to reduce the amount of Pt as CE materials because of their environmental safety, economy, higher surface area and higher chemical stability than those of pristine Pt [38, 46, 47]. Afterwards,

TC14-rGO and TC14-rGO/MWCNTs hybrid was transferred on fluorine-doped tin oxide (FTO) substrate by spray coating method. The sputter coater method was used to coat Pt on its surface. The spray coating method offers a simple process, and it can be easily used in large-scale production [48].

Several semiconductor materials, such as ZnO [49, 50], TiO_2 [51], SnO_2 [52], $SrTiO_3$ [53] and Nb_2O_5 [54], are used as photoanodes. Among these compounds, ZnO and TiO_2 are intensively developed as photoanode materials due to their high chemical and thermal stabilities, direct wide band gap energy of ~ 3.37 eV for ZnO and ~ 3.20 eV for TiO_2 and large surface area [55, 56]. These properties are important for photon energy absorption and photoanode dye adsorption [57]. ZnO presents low cost, high electron mobility (115–155 $cm^2\ V^{-1}\ s^{-1}$) and high electrical conductivity. Thus, this material is suitable for application as photoanode. Several successfully produced ZnO morphology structures are nanowires (NWRs) [58], nanoflakes [59], nanosheets [60] and nanorods (NRs) [61]. According to properties, the aligned ZnO NWRs are widely preferred as photoanode structures due to their larger surface area, stronger emission intensity, higher photocurrent action, higher electrical conductivity and higher η than those of ZnO NRs and nanosheet structures [62, 63].

ZnO NWRs can be synthesised by using sol–gel immersion [64, 65], CVD [66], electrochemical deposition [67] and physical vapour deposition [68]. Among these methods, sol–gel immersion is mostly preferred to fabricate ZnO NWRs because of its low production cost, environmental safety, simple fabrication and ease in controlling the NWR growth [69, 70]. In addition to ZnO, TiO_2 is also developed as photoanode material due to its excellent chemical stability under visible irradiation and nontoxicity [71, 72]. Therefore, ZnO is also composited with TiO_2 as photoanode for DSSC application. The composite of TiO_2 nanoparticles (TiO_2 NPs) with ZnO NWRs can reduce the agglomeration of Zn^{2+}/dye, thereby accelerating electron injection in photoanode [73]. ZnO NWR/TiO_2 NP bilayer is widely applied as a photocatalyst [74] and humidity sensor [75] in water treatment [76] and photoelectrochemical applications [77].

In the current study, we propose a novel combination of rGO synthesised by using customised triple-tail TC14 surfactant with MWCNTs and Pt as CE and ZnO NWR/TiO_2 NP bilayer as photoanode thin film for DSSC application. The TC14-rGO/MWCNTs/Pt hybrid CE presents the highest DSSC performance due to its higher surface area and better electrical conductivity than those of pristine TC14-rGO, TC14-rGO/MWCNTs hybrid and TC14-rGO/Pt hybrid CE thin films. High electrical conductivity, which indicates the fast electron movement of TC14-rGO/MWCNTs/Pt hybrid CE film, is promoted by MWCNTs and Pt compared with that of pristine TC14-rGO. The novel structure of ZnO NWR/TiO_2 NP bilayer photoanode enhances the photoanode performance when using TiO_2 NPs to increase dye adsorption. Consequently, the DSSC efficiency is improved. The CE and photoanode thin films were characterised to investigate their morphological, structural, optical, electrical and DSSC performances by using field emission scanning electron microscopy (FESEM), energy dispersive X-ray (EDX), high-resolution transmission electron microscopy (HRTEM), micro-Raman spectroscopy, X-ray diffraction (XRD), UV–Vis spectroscopy, four-point probe, solar simulator, electrochemical impedance spectroscopy (EIS) and cyclic voltammetry (CV) measurement.

2 Materials and methods

The rGO CE was produced from GO solution via reduction using hydrazine hydrate (Merck, 80% soluble in water) as reducing agent. Prior to rGO production, GO was synthesised by electrochemical exfoliation. Two pieces of graphite rod (99.99%, Good Fellow Company, Germany) with a diameter and length of 10 and 150 mm, respectively, were utilised as sources for GO production. FTO (thickness, 1.1 mm) was used as the substrate. The ZnO NWR/TiO_2 NP bilayer photoanode was fabricated via three steps that involved the fabrication of MgZnO-seeded catalyst, ZnO NWRs and TiO_2 NPs. Firstly, MgZnO was prepared by mixing zinc acetate dehydrate [$Zn(CH_3COO)_2{\bullet}2H_2O$, 99.5%; EMSURE], magnesium nitrate hexahydrate [$Zn(NO_3)_3{\bullet}6H_2O$, 99%; across organic], 2-methoxyethanol ($C_3H_8O_2$) and monoethanolamine (C_2H_7NO). Secondly, the Zn $(NO_3)_2$ and hexamethylenetetramine (HMT) were used to fabricate ZnO NWRs on MgZnO-seeded catalyst. Thirdly, TiO_2 NPs were prepared by mixing commercial titanium (IV) oxide nanopowder (Sigma-Aldrich; particle size, ~ 21 nm), ethanol and titanium tetraisopropoxide (TTIP). Acetonitrile, butyl alcohol and N719 (Solaronix) were used to produce di-tetrabutylammonium cis-bis(isothiocyanato) bis(2,2′-bipyridyl-4,4′-dicarboxylato) ruthenium (II)–N719 dye (Sigma-Aldrich). Dimethyl-propyl-benzimidazole iodide (DMPII) was utilised as electrolyte and prepared from iodolyte AN 50 (Solaronix), veloron nitrile (Sigma-Aldrich), DMPII (Solaronix), butyl pyridine (Sigma-Aldrich) and guanidine thiocyanate (QreC).

2.1 CE fabrication

GO was synthesised by electrochemical exfoliation assisted with customised triple-tail TC14 surfactant. GO was synthesised in a water-based electrolyte solution (0.1 M) containing a surfactant. The graphite rods were then partially immersed in the electrolyte at room temperature for 24 h and connected to a 7 V potential. The produced GO was reduced by utilising hydrazine hydrate as reducing agent to produce rGO. This process was carried out for 24 h at ~ 95 °C, and

the ratio of hydrazine hydrate and GO solution was 1:100. The produced rGO was hybridised with 1 wt.% of MWCNTs. Afterwards, spray coating method was performed to fabricate TC14-rGO and TC14-rGO/MWCNTs hybrid thin films onto FTO substrate that were subsequently annealed for 1 h at 400 °C in ambient argon condition. The sputter coater method was used to fabricate TC14-rGO/Pt hybrid and TC14-rGO/MWCNTs/Pt hybrid thin films with Pt at thickness of ~ 10 nm.

2.2 Photoanode fabrication

ZnO NWR/TiO_2 NP bilayer photoanode was fabricated via three steps, which involved the fabrication of MgZnO-seeded catalyst, ZnO NWRs and TiO_2 NPs. Firstly, MgZnO-seeded catalyst (0.4 M) was prepared using 10 ml of $C_3H_8O_2$, 0.88 g of $Zn(CH_3COO)_2•2H_2O$ and 0.44 g of $Zn(NO_3)_3$. The dopant and stabiliser used were $6H_2O$ and 0.25 ml of C_2H_7NO, respectively. The MgZnO-seeded catalyst was fabricated by spin-coating technique [78, 79] on 2×1 cm^2 FTO substrate for 60 s at 3000 rpm and annealed for 1 h at 500 °C. Secondly, the ZnO NWRs were grown on the surface of the MgZnO-seeded layer by sol–gel immersion. $Zn(NO_3)_2$ (1.4875 g) and HMT (0.7045 g) were mixed with deionised water (200 ml) to prepare 0.025 M of ZnO solution. The ZnO NWRs were grown at 90 °C for 24 h in a water bath and dried at 95 °C for 30 min prior to annealing at 400 °C for 30 min. Thirdly, the TiO_2 paste was coated on the surface of ZnO NWRs by using the squeegee method. Commercial titanium (IV) oxide nanopowder (3.5 g), TTIP (0.5 ml) and ethanol (15 ml) were mixed to prepare the TiO_2 paste. The prepared samples were dried at 150 °C for 10 min prior to annealing at 450 °C for 1 h.

2.3 DSSC fabrication

ZnO NWR/TiO_2 NP bilayer photoanode was immersed in N719 dye (0.3 mM) at room temperature for 24 h. Afterwards, the electrolyte [iodide-tri-iodide (I^-/I^{3-})] from DMPII was injected between the photoanode and CE. The ZnO NWR/TiO_2 NP bilayer photoanode and CE samples (TC14-rGO, TC14-rGO/MWCNTs hybrid, TC14-rGO/Pt hybrid and TC14-rGO/MWCNTs/Pt hybrid) were characterised using FESEM-Hitachi Su8020, EDX-Horiba EMAX, micro-Raman spectroscopy (Renishaw InVia micro-Raman System and Horiba Scientific), XRD (D8 Advance), UV–Vis spectroscopy (Cary 60) and four-point probe measurement (Keithley 2636A). Finally, solar simulator measurement was used to determine the DSSC performance under simulated sunlight illumination (AM 1.0). The DSSCs performance was also determined by using EIS and CV analysis.

3 Result and discussion

The FESEM images of fabricated ZnO NWR/TiO_2 NP bilayer as photoanode material are shown in Fig. 1. The homogeneous grains of MgZnO NPs (diameter, 11–23 nm) were successfully fabricated and used as seeded catalyst layer for ZnO NWR growth (Fig. 1a). Side view observation indicated that the MgZnO-seeded catalyst exhibits high density and thickness of 865–937 nm (Fig. 1c). The high density of hexagonal ZnO NWRs with a small diameter (40–79 nm) is due to the dense and homogeneous grain size of seeded catalyst [80], as observed from the top view (Fig. 1b). In side view, ZnO NWRs (Fig. 1c) present well-aligned ZnO NWRs with a thickness of ~ 1.40–1.60 µm; they grow perpendicular to the MgZnO-seeded catalyst. The applied TiO_2 NPs on ZnO NWRs (Fig. 1d) show high density and homogeneous diameter at 17–27 nm. ZnO NWR/TiO_2 NP bilayer presents a total thickness of ~ 8.58–9.15 µm with the TiO_2 NP thickness of 6.98–7.55 µm (Fig. 1e).

Figure 2 demonstrates the FESEM images and EDX analysis of various fabricated CE thin films. TC14-rGO (Fig. 2a) displays a thin layer at the edge plane (yellow arrow) and less agglomeration and sheet-like structure, which may be due to the improved exfoliation, dispersion and stabilisation promoted by triple-tail TC14 surfactant and successful O functional group reduction [81]. The successful reduction was confirmed by EDX analysis (Fig. 2b), which showed that the TC14-rGO presents lower O content (35.81%) than C content (64.19%). These results are also consistent with the HRTEM analysis results (Fig. 2c, d), in which the TC14-rGO presents four transparent and smooth thin layers caused by the decreased O content in the TC14-rGO produced by reduction [82, 83].

The composite of TC14-rGO with MWCNTs (Fig. 2e) presents a well-dispersed and scattered TC14-rGO/MWCNTs hybrid on the FTO surface. The conjugated network of MWCNTs (red arrows) acts as connecting wires and filler vacancies between TC14-rGO layers (yellow arrows) [84]. The thin layer of TC14-rGO is also observed on the TC14-rGO/MWCNTs hybrid film. The EDX result suggested that the TC14-rGO/MWCNTs hybrid (Fig. 2f) presents a higher atomic percentage of C (75.63%) than that of pristine TC14-rGO (64.19%). This finding may be due to the contribution of MWCNTs hybridised with TC14-rGO. Figure 2g shows the TC14-rGO/Pt hybrid film. The Pt NPs are evenly distributed on the TC14-rGO thin film. The Pt NPs are also distributed homogenously on the surface of TC14-rGO/MWCNTs/Pt hybrid thin film, as shown in Fig. 2i. EDX analysis further confirmed the presence of Pt NPs on the TC14-rGO/Pt and TC14-rGO/MWCNTs/Pt hybrid samples. The atomic percentage of Pt in the

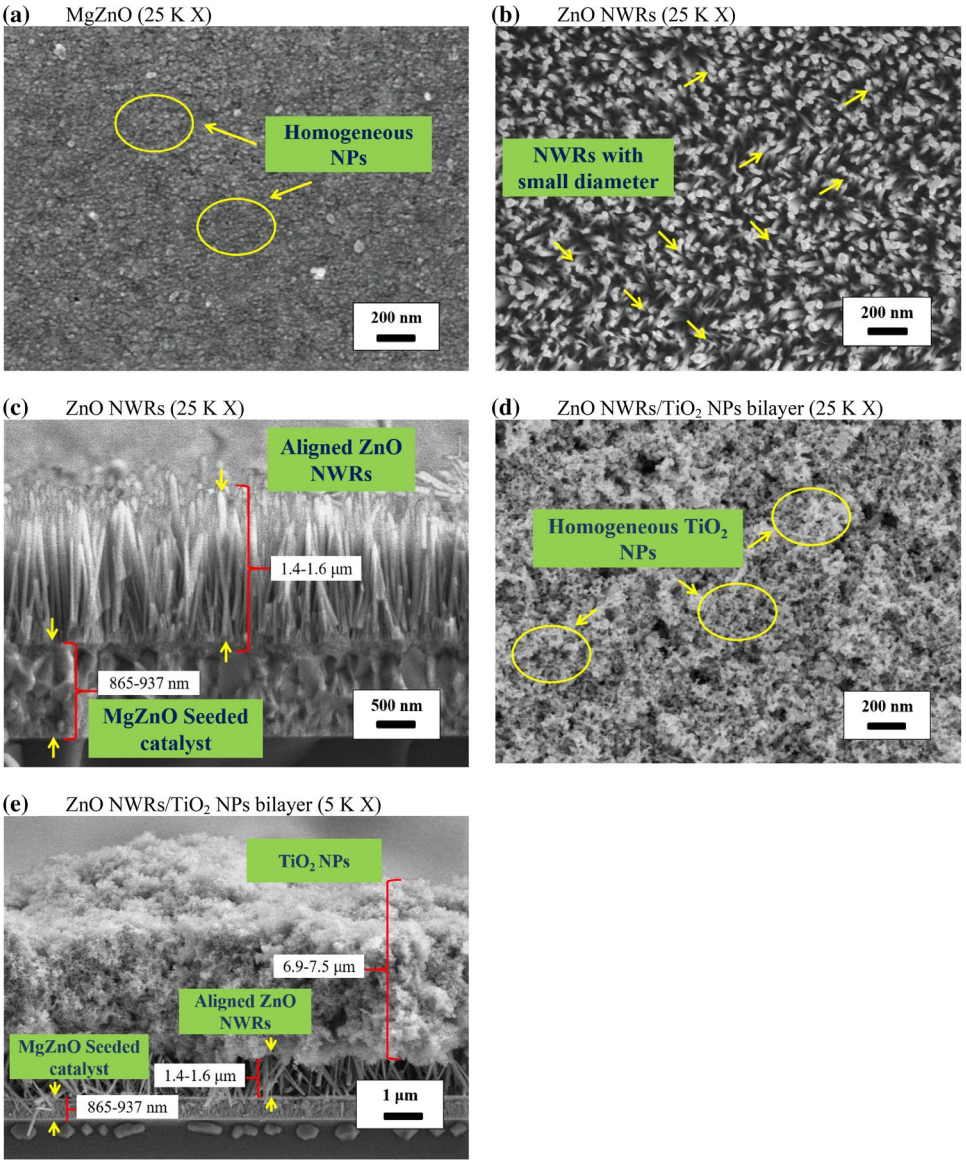

Fig. 1 FESEM images of; **a** MgZnO-seeded catalyst, **b** top, **c** side view of ZnO NWRs, **d** top, **e** side view of ZnO NWRs/TiO_2 NPs bilayer as photoanode films

TC14-rGO/Pt hybrid (Fig. 2h) and TC14-rGO/MWCNTs/Pt hybrid (Fig. 2j) is 0.70% and 1.28%, respectively. The low Pt percentage verified the thin Pt coating (10 nm) on the samples.

The micro-Raman spectra of ZnO NWRs and CE thin films presented in Fig. 3 can be used to investigate the structural properties of the materials [85]. As shown in Fig. 3a, the ZnO NWRs show four peaks, which consist of E_2 high–E_2 low, A_1 (TO), E_2 (high) and E_1 (low) peaks occurring at the range of 300–680 cm^{-1}. The prominent peak of ZnO NWRs at 445 cm^{-1} [E_2 (high)] indicates a wurtzite structure and good ZnO NWR crystallinity. The low peak intensities observed at 333 cm^{-1} (E_2 high–E_2 low) and 382 cm^{-1} (A_1 (TO)) show low defects in the produced sample [86]. The high crystallinity and low O vacancy of ZnO NWRs were proven by the low peak intensity of E_1 (low) at 587 cm^{-1} [68, 87].

The micro-Raman spectra of various CE thin films (Fig. 3b) were used to investigate the disordered structure of carbonaceous materials. The TC14-rGO presents D- and G-bands at 1368 and 1590 cm^{-1}, respectively. The D-band reveals vibrations of sp^3 carbon atoms and indicates the defects in carbon lattice [88]. The vibrations of sp^2-bonded carbon atoms detected by G-band also provide information about the exfoliated sheet layers through electrochemical exfoliation [89]. In the current study, the I_D/I_G ratio from the micro-Raman spectra can be used to determine and predict the existence of defects and the number of the sp^2 domains on the carbon samples [90]. The TC14-rGO shows high I_D/I_G ratio (0.92), which may be attributed to the distortion of

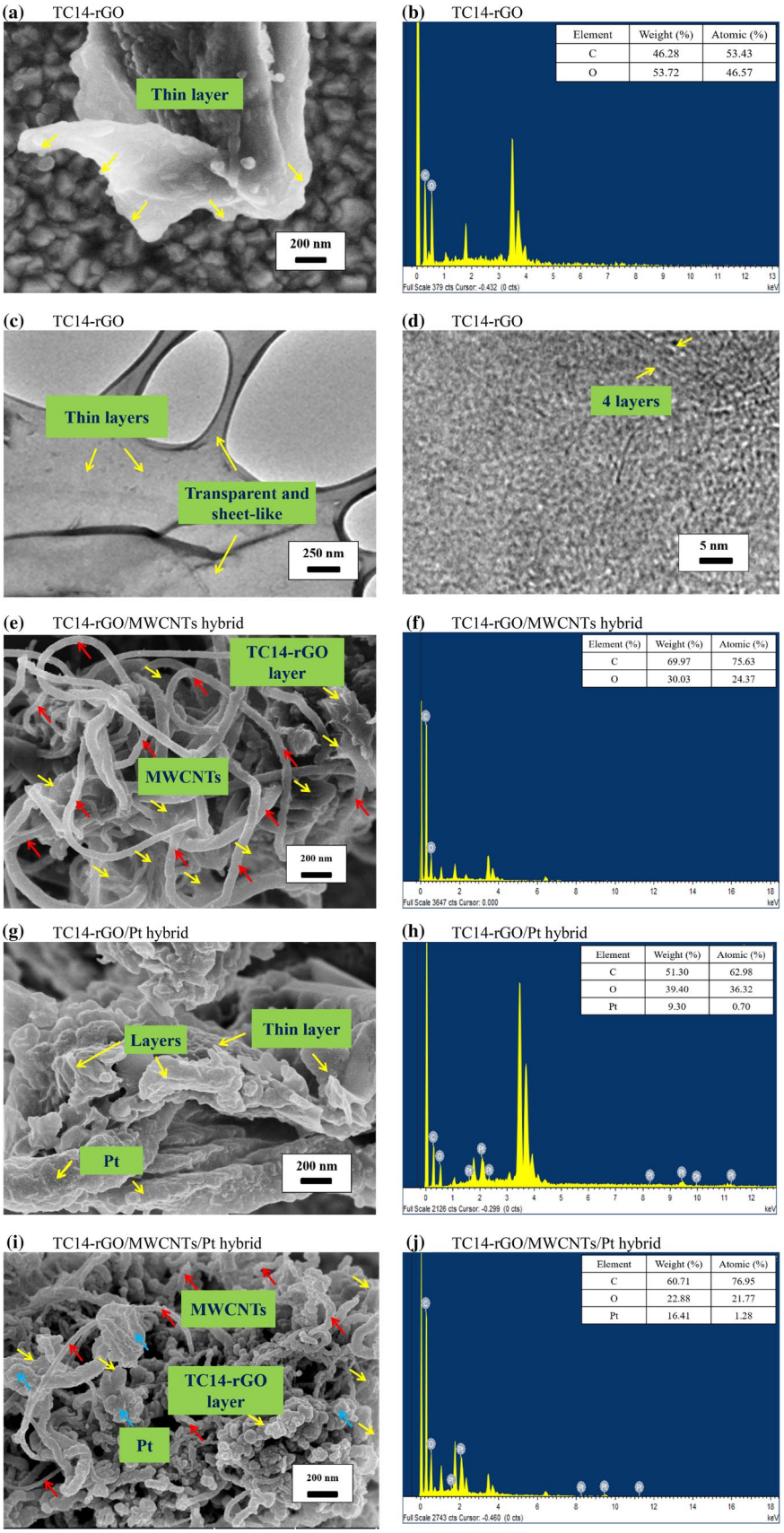

Fig. 2 FESEM images with EDX analysis of **a**, **b** TC14-rGO, HRTEM images of **c**, **d** TC14-rGO, FESEM images with EDX analysis of **e**, **f** TC14-rGO/MWCNTs hybrid, **g**, **h** TC14-rGO/Pt hybrid, **i**, **j** TC14-rGO/MWCNTs/Pt hybrid as CE thin films

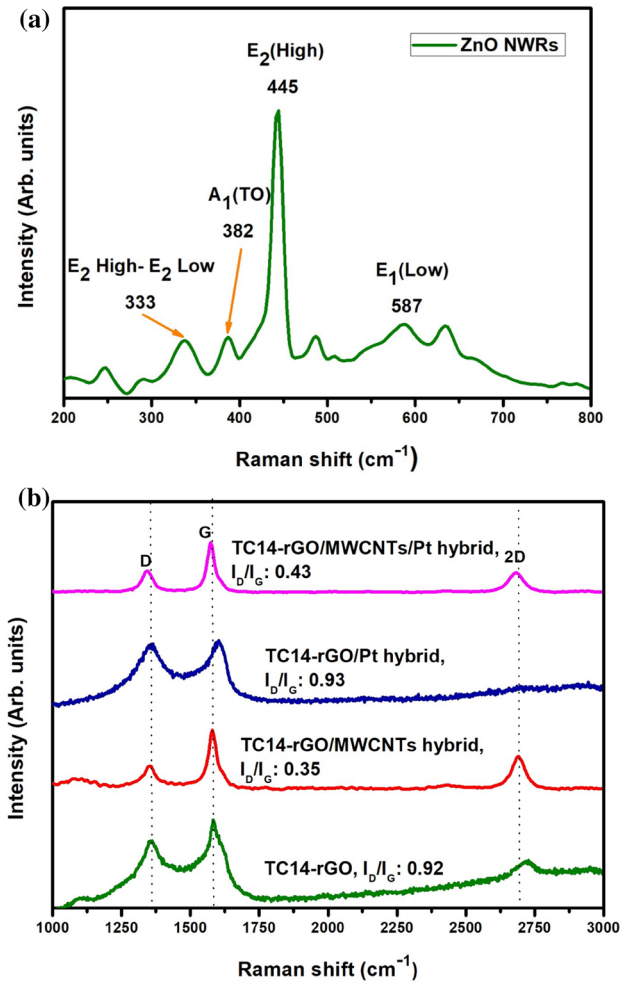

Fig. 3 Micro-Raman spectra of **a** ZnO NWRs, **b** various CE thin films

graphitic domains during the reduction process [91]; this ratio also indicates the amount of new graphitic crystallites [92]. Furthermore, the TC14-rGO shows a 2D-band at 2766 cm^{-1}, which reveals the number of rGO layers [93].

The TC14-rGO/MWCNTs hybrid presents narrower D- (55.04 cm^{-1}) and G-bands (39.60 cm^{-1}) than those of TC14-rGO (325.30 and 66.53 cm^{-1}, respectively). This finding may be due to the narrow D- and G-bands of pristine MWCNTs. The TC14-rGO/MWCNTs hybrid also shows a shifting of D- (1351 cm^{-1}), G- (1580 cm^{-1}) and 2D-bands (2690 cm^{-1}) to a lower wavelength than those of pristine TC14-rGO (1368, 1590 and 2766 cm^{-1}, respectively). This result is considered due to the π-stacking interaction between the TC14-rGO sheets and sidewalls of MWCNTs [94]. The I_D/I_G ratio decreases to ~ 0.35 when the TC14-rGO is composited with the MWCNTs. The low I_D/I_G ratio may be contributed by the low I_D/I_G ratio of pristine MWCNTs, which are consisted of high sp^2 structure [95]. The MWCNTs materials do not exhibit high O content, thereby demonstrating small defects. Additionally, the I_D/I_G ratio decreases. Therefore, with consideration of the I_D/I_G ratio, the TC14-rGO/MWCNTs hybrid may present lower disorder structure than that of pristine TC14-rGO.

The TC14-rGO/Pt hybrid also shows a shifted D-band peak (1362 cm^{-1}) to a lower wavelength than that of TC14-rGO (1368 cm^{-1}). This finding may be due to the good interaction and successful hybridisation between TC14-rGO sheets and Pt [96]. The TC14-rGO composited with Pt presents slightly higher I_D/I_G ratio (0.93) than that of pristine TC14-rGO (0.92). The TC14-rGO/MWCNTs/Pt hybrid also shows lower D- (1343 cm^{-1}) and G-band (1574 cm^{-1}) wavelengths than those of TC14-rGO/MWCNTs hybrid (1351 and 1580 cm^{-1}, respectively). These results indicate the good interaction between TC14-rGO, MWCNTs and Pt in the TC14-rGO/MWCNTs/Pt hybrid sample. The TC14-rGO/MWCNTs/Pt hybrid sample also presents a higher I_D/I_G ratio at of ~ 0.43 than that of TC14-rGO/MWCNTs hybrid (0.35). A summary of the micro-Raman analysis on TC14-rGO, TC14-rGO/MWCNTs hybrid, TC14-GO/Pt hybrid and TC14-rGO/MWCNTs/Pt hybrid as CE materials is presented in Table 1.

Table 1 Micro-Raman spectral analysis of TC14-rGO, TC14-rGO/MWCNTs hybrid, TC14-rGO/Pt hybrid and TC14-rGO/MWCNTs/Pt hybrid as CE thin films

Sample	Raman shift (cm^{-1})			I_D/I_G
	D-band	G-band	2D-band	
TC14-rGO	1368	1590	2766	0.92
TC14-rGO/MWCNTs hybrid	1351	1580	2690	0.35
TC14-rGO/Pt hybrid	1362	1595	2835	0.93
TC14-rGO/MWCNTs/Pt hybrid	1343	1580	2681	0.43

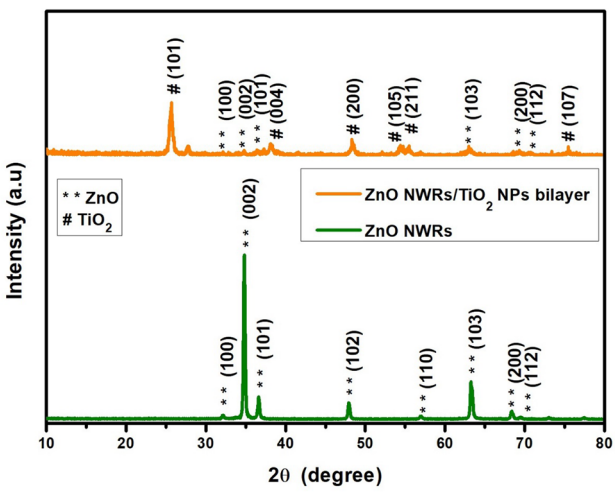

Fig. 4 XRD patterns of ZnO NWRs and ZnO NWRs/TiO_2 NPs bilayer as photoanode materials

The XRD patterns of ZnO NWRs and ZnO NWR/TiO_2 NP bilayer photoanode films are presented in Fig. 4. According to the XRD pattern, the eight diffraction peaks [(100), (002), (101), (102), (110), (103), (200) and (112)] in the ZnO NWRs are in the range of 10°–80°. These peaks confirm the hexagonal-wurtzite structure of ZnO NWRs and show good agreement with that of pure anatase TiO_2 (PDF 01-075-9187). The ZnO NWRs demonstrate the most prominent and intense peak at 34.8° (002), which indicates the perpendicular direction of the as-grown ZnO NWRs to the substrate [97]. The ZnO NWRs also present good crystallinity film due to sharp and high (002) peak intensity. However, the ZnO NWRs also exhibit an increased grain boundary density, which is proven by the appearance of other low-intensity peaks at (100), (110), (200) and (112). This finding may be attributed to the imperfect alignment of ZnO NWRs on the substrate. The full width at half maximum (FWHM) and crystallite size of ZnO NWRs can also be determined from the XRD spectra by using Scherer's equation [98]. The good crystallinity of ZnO NWRs is revealed by the small FWHM value (0.23°) at 2θ (34.84°) and large crystallite size (35 nm). The diffraction peaks of ZnO NWR/TiO_2 NP bilayer show both ZnO and anatase TiO_2 peaks. The XRD pattern shows six diffraction peaks at (101), (004), (200), (105), (211) and (107) and confirms the presence of anatase TiO_2 NP peaks. The ZnO NWR/TiO_2 NP bilayer exhibits a prominent and intense peak at 25.68° (101), which is in good agreement with the XRD pattern of pure anatase TiO_2. The (002) peak of ZnO NWRs can also be observed in the ZnO NWR/TiO_2 NP bilayer films whose intensity is lower than that of pure ZnO NWRs. This finding is due to the interaction between ZnO NWRs and anatase TiO_2 in the ZnO NWR/TiO_2 NP bilayer thin film. The ZnO NWR/TiO_2 NP bilayer presents an increased FWHM and decreased crystallite size at ~ 0.40° and ~ 20 nm, respectively.

The transmittance and band gap energy of various CE thin films were determined by UV–Vis analysis. The TC14-rGO presents the highest transmittance of ~ 92% at λ of 550 nm in the range of 400–800 nm due to its transparent, less agglomerated and thin four-layer sheet film (Fig. 5). This finding may be due to the improved exfoliation promoted by triple-tail TC14 surfactant and the successful reduction process. The TC14-rGO/MWCNTs hybrid shows lower transmittance of ~ 89% than that of pristine TC14-rGO (~ 92%); the difference is attributed to the increased TC14-rGO/MWCNTs hybrid film thickness. The transmittance of the Pt-coated film either on TC14-rGO/Pt hybrid and TC14-rGO/MWCNTs/Pt hybrid decreases to ~ 42% and ~ 34%, respectively. This finding is due to the darker and thicker film of TC14-rGO/Pt hybrid and TC14-rGO/MWCNTs/Pt hybrid than those of pristine TC14-rGO and TC14-rGO/MWCNTs hybrid films from Pt coating (~ 10 nm).

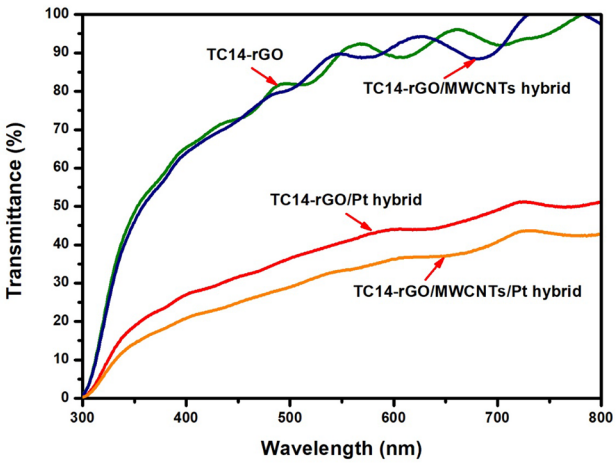

Fig. 5 UV–Vis spectra of various CE thin films

The band gap energy of CE materials can be determined from the transmittance value, which was calculated using the Tauc's plot with linear extrapolation (Fig. 6) [99]. The TC14-rGO (Fig. 6a) shows a high band gap energy of ~ 3.98 eV, which decreases to ~ 3.96 eV after being composited with the MWCNTs (Fig. 6b). This finding is due to the low O content of MWCNTs; it also indicates the better electrical conductivity of the TC14-rGO/MWCNTs hybrid than that of pristine TC14-rGO. The TC14-rGO/Pt and TC14-rGO/MWCNTs/Pt hybrid composites demonstrate decreased band gap energy of ~ 3.92 and 3.89 eV, as obtained from the Tauc's plot (Fig. 6c, d), respectively. The lowest band gap energy of TC14-rGO/MWCNTs/Pt hybrid is attributed to the highest electrical conductivity and the fastest electron movement of CE in DSSC application.

Figure 7 demonstrates the electrical properties of ZnO NWRs and various CE thin films. The ZnO NWRs (Fig. 7a) present high electrical conductivity of ~ 2.9×10^{-1} S cm^{-1}, which may be due to their high surface area. High surface area leads to easy and fast electron movement in the ZnO NWR photoanode film, thereby improving electrical conductivity. The highest electrical conductivity of CE thin film is shown by the TC14-rGO/MWCNTs/Pt hybrid (~ 1.01 S cm^{-1}), TC14-rGO/Pt hybrid (~ 6.6×10^{-1} S cm^{-1}), TC14-rGO/MWCNTs hybrid (~ 6.5×10^{-1} S cm^{-1}) and TC14-rGO (~ 5.6×10^{-1} S cm^{-1}) in sequence, as demonstrated in Fig. 7b. The TC14-rGO composited with the MWCNTs and Pt presents the most excellent electrical conductivity (~ 1.01 S cm^{-1}) among the CE materials, which indicates the fastest electron movement and its suitability as a CE in DSSC application. This result is influenced with the good exfoliation process of triple-tail TC14 surfactant, which further produces high-quality TC14-GO. The lowest band gap energy of TC14-rGO/MWCNTs/Pt hybrid (~ 3.89 eV) and high electrical conductivity of pristine MWCNTs

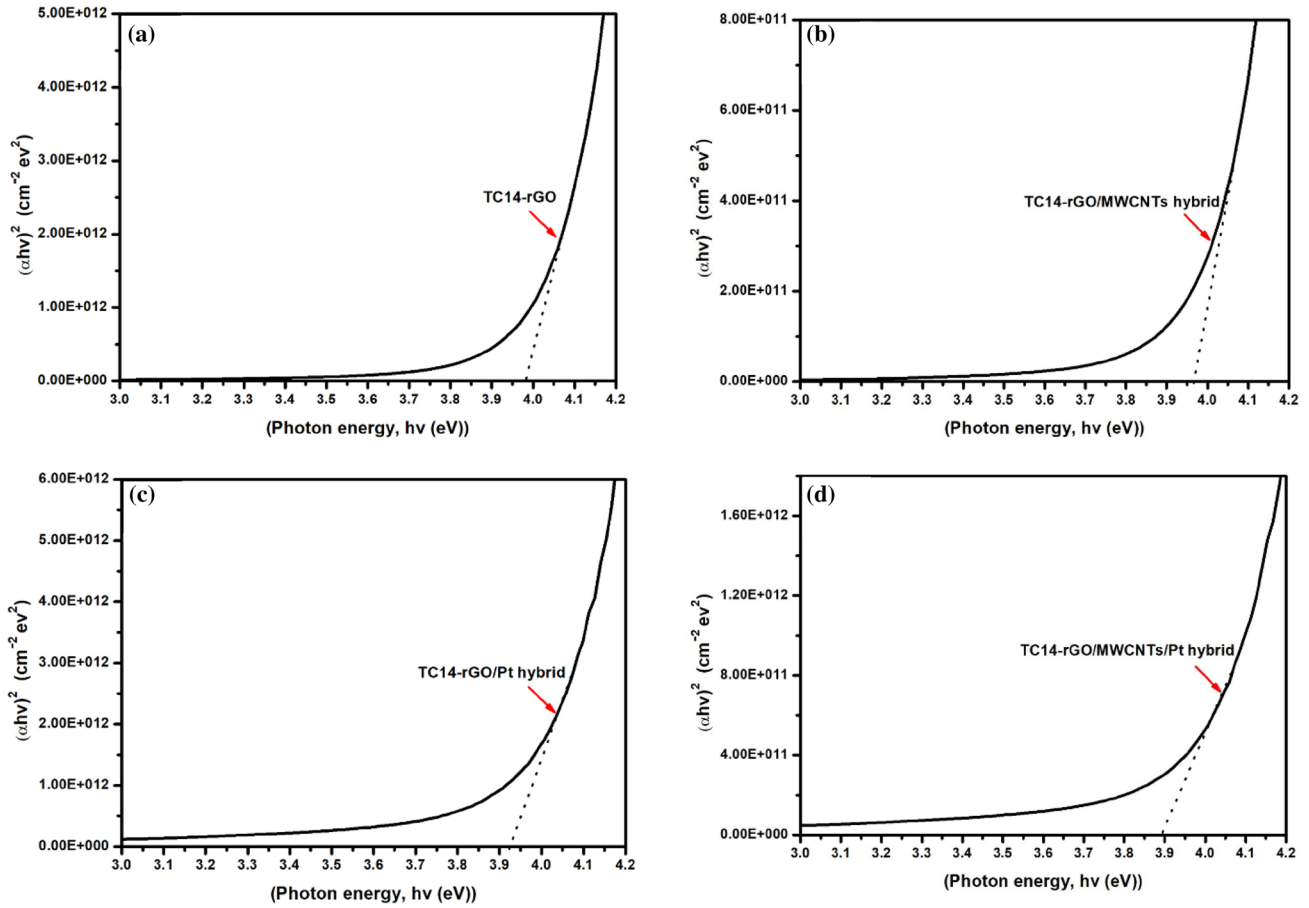

Fig. 6 Band gap energy of **a** TC14-rGO, **b** TC14-rGO/MWCNTs hybrid, **c** TC14-rGO/Pt hybrid, **d** TC14-rGO/MWCNTs/Pt hybrid as CE thin films

(~ 1.37 S cm^{-1}) [100] and Pt (~ 3.87 S cm^{-1}) [17] also affect the highest electrical conductivity of TC14-rGO/MWCNTs/Pt hybrid CE film. The TC14-rGO/MWCNTs hybrid shows higher electrical conductivity (~ 6.5×10^{-1} S cm^{-1}) than that of pristine TC14-rGO (~ 5.6×10^{-1} S cm^{-1}). This result illustrates that MWCNTs improve the electrical properties of TC14-rGO in the TC14-rGO/MWCNTs hybrid sample.

The DSSC performance of ZnO NWR/TiO_2 NP bilayer as photoanode and various CE thin films were plotted as photocurrent density–voltage curves (Fig. 8). Among the CE materials, TC14-rGO/MWCNTs/Pt hybrid exhibits the highest DSSC performance with η, open-circuit voltage (V_{oc}), short-circuit-current density (J_{sc}) and fill factor FF values of 0.084%, 0.608 V, 0.285 mA/cm^2 and 0.397, respectively. The TC14-rGO/MWCNTs/Pt hybrid also demonstrates the highest V_{oc} and J_{sc} values among the CE materials. The highest V_{oc} value of TC14-rGO/MWCNTs/Pt hybrid CE with ZnO NWR/TiO_2 NP bilayer photoanode may be due to the large surface area of MWCNTs and TC14-rGO promoted by triple-tail TC14 surfactant and the high catalytic activity of Pt. Thus, MWCNTs and Pt improve the electrical properties of TC14-rGO. The high surface area of ZnO NWRs and TiO_2 NPs indicates high dye adsorption, which enhances the photo-exciton electrons, increases the electron number in ZnO NWR/TiO_2 NP bilayer photoanode and improves the V_{oc} value. The high electrical conductivity of electron transfer from photoanode materials to the FTO substrate also contributes to the enhancement of V_{oc} value.

The highest J_{sc} value of TC14-rGO/MWCNTs/Pt hybrid is influenced with the lowest band gap energy (~ 3.89 eV) and higher catalytic activity of TC14-rGO/MWCNTs/Pt hybrid than that of other CE materials in the reduction of I_3^- to I^- during the DSSC process, which further improves the DSSC performance. The high surface area of MWCNTs and rGO assisted with triple-tail TC14 surfactant in the TC14-rGO/MWCNTs/Pt hybrid can optimally generate a dye sensitiser after electron injection and accelerate electron movement. Consequently, the DSSC photovoltaic performance is enhanced. The thick ZnO NWR/TiO_2 NP bilayer also indicates optimal dye adsorption, increases the light-harvesting efficiency in the photoanode and enhances the J_{sc} value in DSSC application [55]. The TC14-rGO/Pt hybrid shows

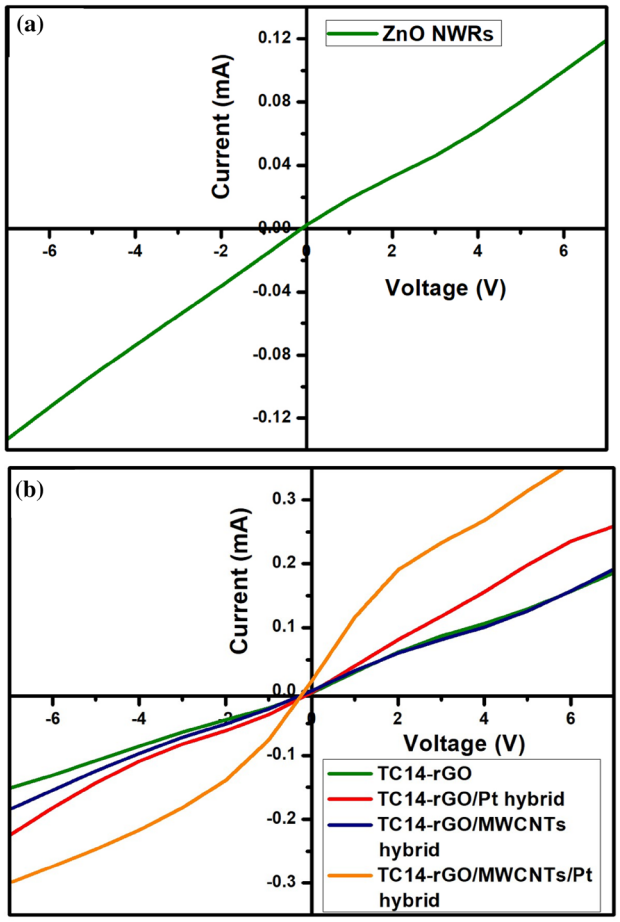

Fig. 7 *I–V* curve of **a** ZnO NWRs, **b** various CE thin films

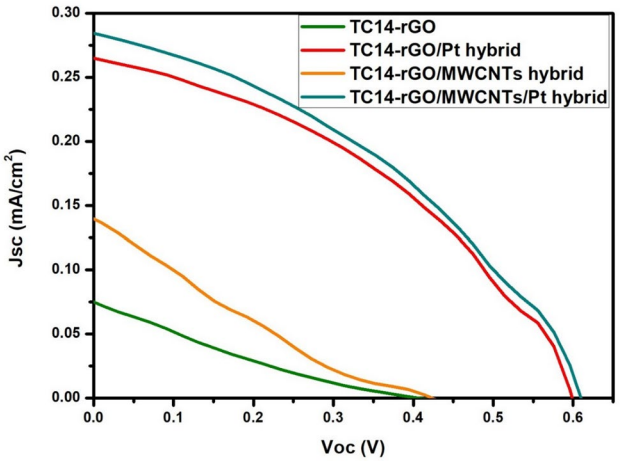

Fig. 8 *J–V* curve of DSSCs by using various CE thin films and ZnO NWRs/TiO_2 NPs bilayer as photoanode thin films

lower η (0.0788%) with J_{sc}, V_{oc} and FF of 0.265 mA/cm^2, 0.597 V and 0.407 than that of the TC14-rGO/MWCNTs/Pt hybrid CE thin film. This result may be due to the high band gap energy (~3.92 eV) and low surface area of TC14-rGO/Pt hybrid, which affect the slow dye regeneration after electron injection and shows a slow route of electrolyte regulation during the DSSC process [4]. According to these results, the utilisation of MWCNTs and Pt enhances the DSSC performance of TC14-rGO CE thin film.

Furthermore, the composite of TC14-rGO with the MWCNTs shows higher η (0.0148%) with J_{sc}, V_{oc} and FF values of 0.140 mA/cm^2, 0.509 V and 0.181 than that of pristine TC14-rGO CE thin film (0.0073%, 0.074 mA/cm^2, 0.418 V and 0.206), respectively. This finding is attributed to the increased surface area and electrical conductivity of TC14-rGO/MWCNTs hybrid ($\sim 6.5 \times 10^{-1}$ S cm^{-1}). The conjugated network of MWCNTs can be used as connecting wires and filler vacancies between agglomeration-free TC14-rGO layers, which accelerate the electron movement during the DSSC process and improve the DSSC performance. The J_{sc}, V_{oc}, FF and η values of various CEs with ZnO NWR/TiO_2 NP bilayer as photoanode in the DSSC application are summarised in Table 2.

The ZnO NWR/TiO_2 NP bilayer as photoanode presents high thickness and surface area, which enhance the dye adsorption promoted by TiO_2 NPs. High photoanode dye adsorption can increase the light-harvesting efficiency and enhance the photo-exciton electrons during DSSC application. The photo-exciton electrons are subsequently converted into electric current, and these results can be observed in the high-energy-conversion efficiency of ZnO NWR/TiO_2 NP bilayer photoanode and TC14-rGO/MWCNTs/Pt hybrid CE. The ZnO NWRs also present high electrical conductivity ($\sim 2.9 \times 10^{-1}$ S cm^{-1}), which results in rapid electron transport in the photoanode and improved the DSSC performance.

The DSSCs performance was also characterised by using EIS and CV analysis. From the EIS analysis, the Nyquist plots are shown in Fig. 9. This analysis can be used to determine the charge transfer resistance (R_{ct1}), interfacial capacitances (C_1) and electron recombination (τ_{oc1}) [101] at the CE materials/electrolyte interface in DSSCs application. The TC14-rGO/MWCNTs/Pt hybrid presents lower R_{ct1} of 58.6 kΩ as compared to TC14-rGO/MWCNTs hybrid (73.1 kΩ), TC14-rGO/Pt hybrid (63.2 kΩ) and TC14-rGO (120 kΩ) due to higher electrical conductivity of TC14-rGO/MWCNTs/Pt hybrid measured by four-point probe analysis. The capacitance of TC14-rGO/MWCNTs/Pt hybrid also shows low C_1 of 7.52 µF. The τ_{oc} was influenced by R_{ct} and C value, with higher R_{ct1} and C_1 causes higher τ_{oc1} value. Therefore, the lowest τ_{oc1} value of the TC14-rGO/MWCNTs/Pt hybrid (440 mΩF) indicates the lowest electron recombination of TC14-rGO/MWCNTs/Pt hybrid thus presents the

Table 2 Summary of DSSC performance with ZnO NWR/TiO_2 NP bilayer as photoanode and various CE thin films

CE thin films	Open-circuit voltage (V_{oc}) (V)	Short-circuit current (J_{sc}) (mA/cm^2)	Fill factor (FF)	Energy conversion efficiency (η) (%)
TC14-rGO	0.418	0.074	0.206	0.0073
TC14-rGO/MWCNTs hybrid	0.509	0.140	0.181	0.0148
TC14-rGO/Pt hybrid	0.597	0.265	0.407	0.0788
TC14-rGO/MWCNTs/Pt hybrid	0.608	0.285	0.397	0.0842

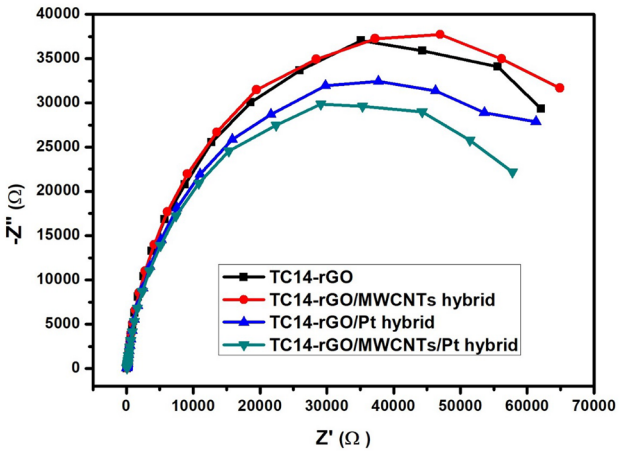

Fig. 9 Nyquist plots of DSSCs with various CE thin film and ZnO NWR/TiO_2 NP bilayer photoanode

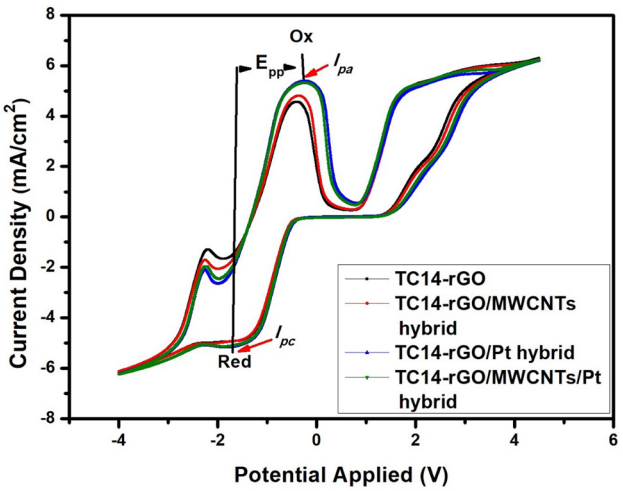

Fig. 10 CV curves of iodide/tri-iodide redox species for CE thin films and ZnO NWR/TiO_2 NP bilayer photoanode

Table 3 Summary fitting results of EIS analysis in DSSCs application with ZnO NWR/TiO_2 NP bilayer as photoanode and various CE thin films

CE thin films	R_s (Ω)	R_{ct1} (kΩ)	C_1 (μF)	τ_{oc1} (mΩF)
TC14-rGO	79	120	12.9	1548
TC14-rGO/Pt hybrid	77.4	63.2	7.29	460
TC14-rGO/MWCNTs hybrid	80.3	73.1	8.04	587
TC14-rGO/MWCNTs/Pt hybrid	79.9	58.6	7.52	440

highest energy conversion efficiency for DSSCs application. The summary fitting results of EIS analysis in DSSCs application with various CE materials and ZnO NWR/TiO_2 NP bilayer as photoanode are listed in Table 3.

The CV analysis was used to investigate the I^-/I_3^- redox couple reaction of CE materials/electrolyte in DSSCs application. Based on CV curve shown in Fig. 10, two sets of peaks [peak-to-peak separation (E_{pp}) and peak current density (I_p)] were obviously seen. The E_{pp} and I_p were known as two important peaks used to estimate the catalytic activity of CE [102]. The I_p value was used to determine the ability of CE material to reduce the I_3^- species because the regeneration of I^- from I_3^- ($I_3^- + 2e^- \rightarrow 3I^-$) in DSSCs application was affected by CE [103]. The TC14-rGO/MWCNTs/Pt hybrid shows lower E_{pp} of 1.02 V as compared to another CE material which demonstrates higher catalytic activity and higher active area of TC14-rGO/MWCNTs/Pt hybrid. Higher catalytic activity of TC14-rGO/MWCNTs/Pt hybrid was believed due to composite of CE materials.

The I_{pa} (oxidation) and I_{pc} (reduction) reaction, which were $3I^- \rightarrow I_3^- + 2e^-$ and $I_3^- + 2e^- \rightarrow 3I^-$, respectively, were also observed from the CV curve. The TC14-rGO/MWCNTs/Pt hybrid shows higher I_{pa} of 5.42 mA/cm^2 as compared to TC14-rGO/MWCNTs hybrid (4.88 mA/cm^2), TC14-rGO/Pt hybrid (5.41 mA/cm^2) and TC14-rGO (4.60 mA/cm^2). Higher I_{pa} of TC14-rGO/MWCNTs/Pt hybrid indicates higher oxidation reaction rate to oxidise the I^- to I_3^- ions [104]. The highest I_{pc} was also presented by TC14-rGO/MWCNTs/Pt hybrid of 0.12 mA/cm^2. The I_{pa} and I_{pc} related to the reaction rate of the catalyst for reducing I_3^- to I^- ions [104]. The highest I_{pa} and I_{pc} of TC14-rGO/MWCNTs/Pt hybrid shows the highest loading of I_3^- to I^- as compared to other CE materials and reveals the increasing of DSSCs performance. Therefore, the TC14-rGO/MWCNTs/Pt hybrid demonstrates the highest energy conversion efficiency as presented in *J–V* curves (see Fig. 8). The details result of

Table 4 Summary of E_{pp}, I_{pa} and I_{pc} of various CE thin film and ZnO NWR/TiO_2 NP bilayer as Photoanode

CE thin films	E_{pp} (V)	I_{pa} (mA/cm^2)	I_{pc} (mA/cm^2)
TC14-rGO	1.08	4.60	5.0
TC14-rGO/Pt hybrid	1.05	5.41	5.05
TC14-rGO/CNTs hybrid	1.07	4.88	5.10
TC14-rGO/CNTs/Pt hybrid	1.02	5.42	5.12

CV analysis of CE thin films in DSSCs application is tabulated in Table 4.

4 Conclusion

The highest DSSC performance is presented by TC14-rGO/MWCNTs/Pt hybrid as CE thin film and ZnO NWR/TiO_2 NP bilayer as photoanode, with η, V_{oc}, J_{sc} and FF values of 0.0842%, 0.618 V, 0.163 mA/cm^2 and 0.387, respectively. The TC14-rGO/MWCNTs/Pt hybrid CE also shows the highest V_{oc} value, which is due to the high surface area of MWCNTs and TC14-rGO promoted by triple-tail TC14 surfactant and the high catalytic activity of Pt. This material can optimally generate a dye sensitiser after electron injection, accelerate electron movement and consequently enhance the DSSC photovoltaic performance. The highest V_{oc} value is also influenced with the decreased charge recombination, increased number of electron in ZnO NWR/TiO_2 NP bilayer photoanode and the high electrical conductivity of electron transfer from photoanode materials to the FTO substrate. The lowest band gap energy (~3.89 eV), lowest charge transfer resistance (R_{ct1}) (58.6 kΩ), lowest electron recombination (τ_{oc1}) (440 mΩF) and high catalytic activity of TC14-rGO/MWCNTs/Pt hybrid in the reduction of I_3^- to I^- during the DSSC process contribute to the highest J_{sc} value, which further improves the DSSC performance. This finding shows that the composite of agglomerated-free rGO assisted with customised triple-tail TC14 surfactant with the MWCNTs and Pt improves the CE properties and enhances the DSSC performance.

Acknowledgements The authors would like to thank the TWAS-COMSTECH Joint Research Grant (Grant Code 2017-0001-102-11) and Fundamental Research Grand Scheme (Grant Code 2015-0154-102-02) for providing financial support.

References

1. O'Regan B, Gratzel M (1991) A low-cost, high-efficiency solar cell based on dye-sensitized colloidal titanium dioxide films. Nature 6346(353):737–740
2. Hug H, Bader M, Mair P, Glatzel T (2014) Biophotovoltaics: natural pigments in dye-sensitized solar cells. Appl Energy 115:216–225
3. Yang JH, Bark CW, Kim KH, Choi HW (2014) Characteristics of the dye-sensitized solar cells using TiO_2 nanotubes treated with $TiCl_4$. Materials 4(90):3522–3532
4. Xue Y, Liu J, Chen H, Wang R, Li D, Qu J, Dai L (2012) Nitrogen-doped graphene foams as metal-free counter electrodes in high-performance dye-sensitized solar cells. Chem Int Ed 51(48):12124–12127
5. Tsai C, Chen C, Hsiao Y, Chuang P (2014) Investigation of graphene nanosheets as counter electrodes for efficient dye-sensitized solar cells. Org Electron 17:57–65
6. Kole M, Dey TK (2013) Investigation of thermal conductivity, viscosity and electrical conductivity of graphene based nanofluids. J Appl Phys 113(8):084307-1–084307-8
7. Parvez K, Wu Z, Li R, Liu X, Graf R (2014) Exfoliation of graphite into graphene in aqueous solutions. J Am Chem Soc 136:6083–6091
8. Ovid'ko I (2013) Mechanical properties of graphene. Rev Adv Mater Sci 34:1–11
9. Li Z, Song B, Wu Z, Lin Z, Yao Y, Moon KS, Wong CP (2015) 3D porous graphene with ultrahigh surface area for microscale capacitive deionization. Nano Energy 11:711–718
10. Nur S, Mohd A, Isa I, Hashim N (2014) A review of glucose biosensors based on graphene/metal oxide nanomaterials. Anal Lett 47:1821–1834
11. Chang LH, Hsieh CK, Hsiao MC, Chiang JC, Liu PI, Ho KK, Ma CCM, Yen MY, Tsai MC, Tsai CH (2013) A graphene-multi-walled carbon nanotube hybrid supported on fluorinated tin oxide as a counter electrode of dye-sensitized solar cells. J Power Sources 222:518–525
12. Miao X, Tongay S, Petterson MK, Berke K, Rinzler AG, Appleton BR, Hebard AF (2012) High efficiency graphene solar cells by chemical doping. Nano Lett 12:6–11
13. Kim KS, Zhao Y, Jang H, Lee SY, Kim JM, Kim KS, Ahn JH, Kim P, Choi JY, Hong BH (2008) Large-scale pattern growth of graphene films for stretchable transparent electrodes. Nature 457(7230):706–710
14. Ma J, Shen W, Li C, Yu F (2015) Light reharvesting and enhanced efficiency of dye-sensitized solar cells based 3D-CNT/graphene counter electrodes. J Mater Chem A 3:12307–12313
15. Wang H, Hu YH (2012) Graphene as a counter electrode material for dye-sensitized solar cells. Energy Environ Sci 5:8182–8188
16. Murakami TN, Ito S, Wang Q, Nazeeruddin MK, Bessho T, Cesar I, Liska P, Baker RH, Comte P, Pechy P, Gratzel M (2006) Highly efficient dye-sensitized solar cells based on carbon black counter electrodes. J Electrochem Soc 153(12):A2255–A2261
17. Suriani AB, Fatiatun, Mohamed A, Muqoyyanah Hashim N, Rosmi MS, Mamat MH, Malek MF, Salifairus MJ, Khalil HPSA (2018) Reduced graphene oxide/platinum hybrid counter electrode assisted by custom-made triple tails surfactant and zinc oxide/titanium dioxide bilayer nanocomposite photoanode for enhancement of DSSCs photovoltaic performance. Opt Int J Light Electron Opt 161:70–83
18. Bykkam S, Rao V, Chakra S, Thunugunta T (2013) Synthesis and characterization of graphene oxide and its antibacterial activity against klebseilla and staphylococus. Inter J Adv Biotechnol Res 4(1):1005–1009
19. Alanyalioglu M, Segura JJ, Sole JO, Pastor NC (2011) The synthesis of graphene sheets with controlled thickness and order using surfactant-assisted electrochemical processes. Carbon 50:142–152
20. Chen J, Yao B, Li C, Shi G (2013) An improved Hummers method for eco-friendly synthesis of graphene oxide. Carbon 64(1):225–229

21. Yu P, Lowe SE, Simon GP, Zhong YL (2015) Electrochemical exfoliation of graphite and production of functional graphene. Curr Opin Colloid Interface Sci 20(5–6):329–338
22. Parvez K, Li R, Puniredd SR, Hernandez Y, Hinkel F, Wang S, Feng X, Mullen K (2013) Electrochemically exfoliated graphene as solution-processable, highly conductive electrodes for organic electronics. ACS Nano 7(4):3598–3606
23. Liu J, Duan Y, Zhou X, Lin Y (2013) Improved synthesis of graphene flakes from the multiple electrochemical exfoliation of graphite rod. Nano Energy 2(3):377–386
24. Suriani AB, Muqoyyanah, Mohamed A, Mamat MH, Hashim N, Isa IM, Malek MF, Kairi MI, Mohamed AR, Ahmad MK (2017) Improving the photovoltaic performance of DSSCs using a combination of mixed-phase TiO_2 nanostructure photoanode and agglomerated free reduced graphene oxide counter electrode assisted with hyperbranched surfactant. Opt Int J Light Electron Opt 158:522–534
25. Mohamed A, Ardyani T, Suriani AB, Brown P, Hollamby M, Sagisaka M, Eastoe J (2016) Graphene-philic surfactants for nanocomposites in latex technology. Adv Colloid Interface Sci 230:54–69
26. Uddin E, Kuila T, Nayak GC, Kim NH, Ku BC, Lee JH (2013) Effects of various surfactants on the dispersion stability and electrical conductivity of surface modified graphene. J Alloys Compd 562:134–142
27. Zeng BQ, Cheng J, Tang L, Liu X, Liu Y, Li J (2010) Self-assembled graphene–enzyme hierarchical nanostructures for electrochemical biosensing. Adv Funct Mater 20:3366–3372
28. Kakaei K, Hasanpour K (2014) Synthesis of graphene oxide nanosheets by electrochemical exfoliation of graphite in cetyltrimethylammonium bromide and its application for oxygen reduction. J Mater Chem A Mater Energy Sustain 2:15428–15436
29. Stankovich S, Piner RD, Chen X, Wu N, Nguyen T, Ruoff RS (2006) Stable aqueous dispersions of graphitic nanoplatelets via the reduction of exfoliated graphite oxide in the presence of poly (sodium 4-styrenesulfonate). J Mater Chem 16:155–158
30. Mohamed A, Anas AK, Suriani AB, Ardyani T, Zin WMW, Ibrahim S, Sagisaka M, Brown P (2015) Enhanced dispersion of multiwall carbon nanotubes in natural rubber latex nanocomposites by surfactants bearing phenyl groups. J Colloid Interface Sci 455:179–187
31. Mohamed A, Anas AK, Suriani AB, Aziz AA, Sagisaka M, Brown P, Eastoe J, Kamari A, Hashim N, Isa IM (2014) Stabilised by highly branched hydrocarbon surfactants and dispersed in natural rubber latex nanocomposites. Colloid Polym Sci 292:3013–3023
32. Chua CK, Pumera M (2014) Chemical reduction of graphene oxide: a synthetic chemistry viewpoint. Chem Soc Rev 43:291–312
33. Xie X, Zhao K, Xu X, Zhao W, Liu S, Zhu Z, Li M, Shi Z, Shao Y (2010) Study of heterogeneous electron transfer on the graphene/self-assembled monolayer modified gold electrode by electrochemical approaches. J Phys Chem C 114:14243–14250
34. Wang Y, Zhang P, Liau CF, Zhan L, Li YF, Huang CZ (2012) Green and easy synthesis of biocompatible graphene for use as an anticoagulant. RSC Adv 2:2322–2328
35. Liu J, Fu S, Yuan B, Li Y, Deng Z (2010) Toward a universal "adhesive nanosheet" for the assembly of multiple nanoparticles based on a protein-induced reduction/decoration of graphene. J Am Chem Soc 132:7279–7281
36. Zhang S, Shao Y, Liao H, Engelhard MH, Yin G, Lin G (2011) Polyelectrolyte-induced reduction of exfoliated graphite oxide: a facile route to synthesis of soluble graphene. ACS Nano 5(3):1785–1791
37. Lee Y, Zhang Y, Lay S, Ng G, Kartawidjaja FC, Wang J (2009) Hydrothermal growth of vertical ZnO nanorods. J Mater Ceram Soc 92(9):1940–1945
38. Orlita M, Faugeras C, Plochocka P, Neugebaurer P, Martinez G, Maude DK, Barra AL, Sprinkle M, Borger C, Heer WAD, Potemski M (2008) Approaching the Dirac point in high-mobility multilayer epitaxial graphene. Phys Rev Lett 101(26):267601-1–267601-4
39. Pop E, Mann D, Wang Q, Goodson K, Dai H (2006) Thermal conductance of an individual single-wall carbon nanotube above room temperature. Nano Lett 6(1):96–100
40. Suriani AB, Alfarisa S, Mohamed A, Isa IM, Kamari A, Hashim N (2014) Quasi-aligned carbon nanotubes synthesised from waste engine oil. Mater Lett 139:220–223
41. Suriani AB, Dalila AR, Mohamed A, Mamat MH, Salina M, Rosmi MS, Rosly J, Nor RM, Rusop M (2013) Vertically aligned carbon nanotubes synthesized from waste chicken fat. Mater Lett 101:61–64
42. Suriani AB, Nor R, Rusop M (2010) Vertically aligned carbon nanotubes synthesized from waste cooking palm oil. J Cer Soc Jpn 118:963–968
43. Zobir SAM, Suriani AB, Abdullah S, Zainal Z, Sarijo SH, Rusop M (2012) Raman spectroscopic study of carbon nanotubes prepared using Fe/ZnO-palm olein-chemical vapour deposition. J Nanomat 2012(451473):1–6
44. Jackson P, Jacobsen NR, Baun A, Bikerdal R, Kuhnel D, Jensen KA, Vogel A, Wallin H (2013) Bioaccumulation and ecotoxicity of carbon nanotubes bioaccumulation and ecotoxicity of carbon nanotubes. Chem Cen J 7(154):1–21
45. Azmina MS, Suriani AB, Falina AN (2012) Temperature effects on the production of carbon nanotubes from palm oil by thermal chemical vapor deposition method. Adv Mat Res 364:359–362
46. Zhang DW, Li XD, Li HB, Chen S, Sun Z, Yin ZJ, Huang SM (2011) Graphene-based counter electrode for dye-sensitized solar cells. Carbon 49:5382–5388
47. Lee WJ, Ramasamy E, Lee DY, Song JS (2009) Efficient dye-sensitized solar cells with catalytic multiwall carbon nanotube counter electrodes. ACS App Mat Inter 6:1145–1149
48. Pham VH, Cuong TV, Hur SH, Shin EW, Kim JS, Chung J, Kim EJ (2010) Fast and simple fabrication of a large transparent chemically-converted graphene film by spray-coating. Carbon 48(7):1945–1951
49. Omar A, Abdullah H (2014) Electron transport analysis in zinc oxide-based dye-sensitized solar cells: a review. Renew Sustain Energy Rev 31:149–157
50. Rahman MYA, Umar AA, Taslim R, Roza L, Saad SKM, Salleh MM (2014) TiO_2 and ZnO thin film nanostructure for photoelectrochemical cell application: a Brief Review. Int J Electroactive Mater 2:4–7
51. Arunachalam A, Dhanapandian S, Manoharan C, Sridhar R (2015) Spectrochimica acta part a: molecular and biomolecular spectroscopy characterization of sprayed TiO_2 on ITO substrates for solar cell applications. Spectrochim Acta Part A Mol Biomol Spectrosc 149:904–912
52. Snaith HJ, Ducati C (2010) SnO_2-based dye sensitized hybrid solar cells exhibiting near unity absorbed photon-to-electron conversion efficiency. Nano Lett 10:1259–1265
53. Kim CW, Suh SP, Choi MJ, Kang YS, Kang YS (2013) Fabrication of $SrTiO_3$–TiO_2 heterojunction photoanode with enlarged pore diameter for dye-sensitized solar cells. J Mater Chem A 1:11820–11827
54. Jin X, Liu C, Xu J, Wang Q, Chen D (2014) Size-controlled synthesis of mesoporous Nb_2O_5 microspheres for dye senistized solar cells. RSC Adv 4:35546–35553
55. Yang G, Miao C, Bu Z, Wang Q, Guo W (2013) Seed free and low temperature growth of ZnO nanowires in mesoporous TiO_2

film for dye-sensitized solar cells with enhanced photovoltaic performance. J Power Sources 233:74–78
56. Safitri RN, Suriani AB, Alfarisa S, Mohamed A, Hashim N, Kamari A, Isa IM, Mahmood MR, Mohamed AR (2015) Zinc oxide/carbon nanotubes nanocomposite: synthesis methods and potential applications. Adv Mater Res 1109:45–49
57. Lee Y, Chae J, Kang M (2010) Comparison of the photovoltaic efficiency on DSSC for nanometer sized TiO_2 using a conventional sol–gel and solvothermal methods. J Ind Eng Chem 16(4):609–614
58. Fan J, Hao Y, Munuera C, Hernandez MG, Guell F, Johansson EMJ, Boschloo G, Hagfeldt A, Cabot A (2013) Influence of the annealing atmosphere on the performance of ZnO nanowire dye-sensitized solar cells influence of the annealing atmosphere on the performance of ZnO nanowire dye-sensitized solar cells. J Phys Chem C 17:6349–16356
59. Mou J, Zhang W, Fan J, Deng H, Chen W (2011) Facile synthesis of ZnO nanobullets/nanoflakes and their applications to dye-sensitized solar cells. J Alloys Compd 509(3):961–965
60. Li Z, Zhou Y, Xue G, Yu T, Liu J, Zhou Z (2012) Fabrication of hierarchically assembled microspheres consisting of nanoporous ZnO nanosheets for high-efficiency dye-sensitized solar cells. J Mater Chem 22:14341–14345
61. Wu Y, Liu D, Yu N, Liu Y, Liang H, Du G (2013) Structure and electrical characteristics of zinc oxide thin films grown on si (111) by metal–organic chemical vapor deposition. J Mater Sci Technol 29(9):830–834
62. Fan Z, Lu JG (2005) Zinc oxide nanostructures: synthesis and properties. J Nanosci Nanotechnol 5(10):1561–1573
63. Muskens OL, Rivas JG, Algra RE, Bakkers EPAM, Lagendijk A (2008) Design of light scattering in nanowire materials for photovoltaic applications. Nano Lett 8(9):2638–2642
64. Malek MF, Hafiz MH, Soga T, Rahman SA, Suriani AB, Ismail AS, Alrokayan SAH, Khan HA, Mahmood MR (2016) Thickness-controlled synthesis of vertically aligned c-axis oriented ZnO nanorod arrays: effect of growth time via novel dual sonication sol–gel process. J Appl Phys 55:011AE5-1–011AE5-6
65. Suriani AB, Safitri RN, Mohamed A, Alfarisa S, Isa IM, Kamari A, Hashim N, Ahmad MK, Malek MF, Rusop M (2015) Enhanced field electron emission of flower-like zinc oxide on zinc oxide nanorods grown on carbon nanotubes. Mater Lett 149:66–69
66. Lu L, Chen J, Li L, Wang W (2012) Direct synthesis of vertically aligned ZnO nanowires on FTO substrates using a CVD method and the improvement of photovoltaic performance. Nanoscale Res Lett 7(293):1–8
67. Lupan O, Pauporte T, Viana B, Tiginyanu IM, Ursaki VV, Cortes R (2010) Epitaxial electrodeposition of ZnO nanowire arrays on p-GaN for efficient UV-light emitting diode fabrication. ACS Appl Mater Inter 2(7):2083–2090
68. Zhang Y, Ram MK, Stefanakos EK, Goswami DY (2012) Synthesis, characterization and applications of ZnO nanowires. J Nanomat 2012:1–22
69. Caglar Y (2013) Sol–gel derived nanostructure undoped and cobalt doped ZnO: structural, optical and electrical studies. J Alloys Compd 560:181–188
70. Malek MF, Mamat MH, Khusami Z, Sahdan MZ, Musa MZ, Zainun AR, Suriani AB, Sin NDM, Hamid SBA, Rusop M (2014) Sonicated sol–gel preparation of nanoparticulate ZnO thin films with various deposition speeds: the highly preferred *c*-axis (002) orientation enhances the final properties. J Alloys Compd 582:12–21
71. Chai S, Lau T, Dayou J, Sipaut CS, Mansa RF (2014) Development in photoanode materials for high efficiency dye sensitized solar cells. Int J Renew Energy Res 4(3):37
72. Narayan MR (2012) Review:dye sensitized solar cells based on natural photosensitizers. Renew Sustain Energy Rev 16(1):208–215
73. Lou Y, Yuan S, Zhao Y, Hu P, Wang Z, Zhang M, Shi L, Li D (2013) A simple route for decorating TiO_2 nanoparticle over ZnO aggregates dye-sensitized solar cell. Chem Eng J 229:190–196
74. Zhou Q, Wen JZ, Zhao P, Anderson WA (2017) Synthesis of vertically-aligned zinc oxide nanowires and their application as a photocatalyst. Nanomater 7(9):1–13
75. Yadav BC, Pandey NK, Srivastava AK, Sharma P (2007) Optical humidity sensors based on titania films fabricated by sol–gel and thermal evaporation methods. Meas Sci Technol 18:254–260
76. Chorfi H, Saadoun M, Bousselmi L, Bessais B (2012) TiO_2–ITO and TiO_2–ZnO nanocomposites: application on water treatment. EPJ Web Con 29:00015-1–00015-7
77. Samad NA, Lai CW, Lau KS, Hamid SBA (2016) Efficient solar-induced photoelectrochemical response using coupling semiconductor TiO_2–ZnO nanorod film. Materials 9(937):1–21
78. Suriani AB, Dalila AR, Mohamed A, Mamat MH, Malek MF, Soga T, Tanemura M (2016) Fabrication of vertically aligned carbon nanotubes-zinc oxide nanocomposites and their field electron emission enhancement. Mater Des 90:185–195
79. Suriani AB, Safitri RN, Mohamed A, Alfarisa S, Malek MF (2016) Synthesis and field electron emission properties of waste cooking palm oil-based carbon nanotubes coated on different zinc oxide nanostructures. J Alloys Compd 656:368–377
80. Rusli NI, Tanikawa M, Mahmood MR, Yasui K (2012) Growth of high-density zinc oxide nanorods on porous silicon by thermal evaporation. Materials 5:2817–2832
81. Kaniyoor A, Ramaprabhu S (2011) Thermally exfoliated graphene based counter electrode for low cost dye sensitized solar cells. J Appl Phys 109:124308-1–124308-6
82. Hu J, Li H, Wu Q, Zhao Y, Jiao Q (2014) Synthesis of TiO_2 nanowire/reduced graphene oxide nanocomposites and their photocatalytic performances. Chem Eng J 263:144–150
83. Safavi A, Tohidi M, Mahyari FA, Shahbaazi H (2012) One-pot synthesis of large scale graphene nanosheets from graphite–liquid crystal composite via thermal treatment. J Mater Chem 22:3825–3831
84. Zhu G, Pan L, Lu T, Sun Z (2011) Electrophoretic deposition of reduced graphene-carbon nanotubes composite films as counter electrodes of dye-sensitized solar cells. J Mater Chem 21:14869–14875
85. Ahmed F, Kumar S, Arshi N, Anwar MS, Prakash R (2011) Growth and characterization of ZnO nanorods by microwave-assisted route: green chemistry approach. Adv Mater Lett 2(3):183–187
86. Devaraj R, Karthikeyan K, Jeyasubramanian K (2013) Synthesis and properties of ZnO nanorods by modified Pechini process. Appl Nanosci 3(1):37–40
87. Marie M, Mandal S, Manasreh O (2015) An electrochemical glucose sensor based on zinc oxide nanorods. Sensors 15:18714–18723
88. Kumar R, Singh RK, Singh DP, Vaz AR, Yadav RR, Rout CS, Moshkalev SA (2017) Synthesis of self-assembled and hierarchical palladium CNTs-reduced graphene oxide composites for enhanced field emission properties. Mater Des 122:110–117
89. Chen X, Pe D, Wu H, Zhao X, Zhang J, Cheng K, Wu P, Mu S (2015) Platinized graphene/ceramics nano-sandwiched architectures and electrodes with outstanding performance for PEM fuel cells. Sci Rep 5(16246):1–10
90. Tuinstra F, Koenig JL (1970) Raman spectrum of graphite Raman spectrum of graphite. J Chem Phys 53(3):1126–1130
91. Stankovich S, Dikin DA, Piner RD, Kohlhaas KA, Kleinhammes A, Jia Y, Wu Y, Nguyen ST, Ruoff RS (2007) Synthesis of

graphene-based nanosheets via chemical reduction of exfoliated graphite oxide. Carbon 45:1558–1565
92. Liu H, Zhang L, Guo Y, Cheng C, Yang L, Jiang L, Yu G, Hu W, Liu Y, Zhu D (2013) Reduction of graphene oxide to highly conductive graphene by Lawesson's reagent and its electrical applications. J Mat Chem C 1:3104–3109
93. Low CTJ, Walsh FC, Chakrabarti MH, Hashim MA, Hussain MA (2013) Electrochemical approaches to the production of graphene flakes and their potential applications. Carbon 54:1–11
94. Hong X, Chen Y, Wu PZ, Zheng H (2015) Simple, effective fabrication of layered carbon nanotube/graphene hybrid field emitters by electrophoretic deposition. J Vac Sci Technol B 33(1):011802-1–011802-8
95. Kumar K, Kim YS, Li X, Ding J, Fisher FT, Yang EH (2013) Chemical vapor deposition of carbon nanotubes on monolayer graphene substrates: reduced etching via suppressed catalytic hydrogenation using C_2H_4. Chem Mater 25(19):3874–3879
96. Yang B, Bin D, Wang H, Zhu M, Yang P, Du Y (2015) Colloids and surfaces A: physicochemical and engineering aspects high quality pt–graphene nanocomposites for efficient electrocatalytic nitrite sensing. Colloids Surfaces A Physicochem Eng Asp 481:43–50
97. Manthina V, Baena JPC, Liu G, Agrios AG (2012) ZnO–TiO_2 nanocomposite films for high light harvesting efficiency and fast electron transport in dye-sensitized solar cells. J Phys Chem C 116:23864–23870
98. Shabannia R (2015) Vertically aligned ZnO nanorods on porous silicon substrates: effect of growth time. Prog Nat Sci Mater Int 25(2):95–100
99. Tauc J, Grigorovici R, Vancu A (1966) Optical properties and electronic structure of amorphous germanium. Phys Stat Sol 15:627–637
100. Mathur RB, Pande S, Singh BP, Dhami TL (2008) Electrical and mechanical properties of multi-walled carbon nanotubes reinforced PMMA and PS composites. Polym Comp 29(7):717–727
101. Tao X, Ruan P, Zhang X, Sun Zhou X (2015) Microsphere assembly of TiO_2 mesoporous nanosheets with highly exposed (101) facets and application in light-trapping quasi-solid-state dye-sensitized solar cell. Nanoscale 7:3539–3547
102. Gong J, Liang J, Sumathy K (2012) Review on dye-sensitized solar cells (DSSCs): fundamental concepts and novel materials. Renew Sustain Energy Rev 16(8):5848–5860
103. Roy-mayhew JD, Bozym DJ, Punckt C, Aksay IA (2010) Functionalized graphene as a catalytic solar cells. ACS Nano 4(10):6203–6211
104. Yue G, Ma X, Zhang W, Li F, Wu J, Li G (2015) A highly efficient flexible dye-sensitized solar cell based on nickel sulfide/platinum/titanium counter electrode. Nanoscale Res 10(1):1–9